An outer-pore gate modulates the pharmacology of the TMEM16A channel

Ria L. Dinsdale[a,b] (ID), Tanadet Pipatpolkai[c,d,1] (ID), Emilio Agostinelli[a,1] (ID), Angela J. Russell[a,b], Phillip J. Stansfeld[c,e,2] (ID), and Paolo Tammaro[a,2] (ID)

[a]Department of Pharmacology, University of Oxford, Oxford OX1 3QT, United Kingdom; [b]Department of Chemistry, University of Oxford, Oxford OX1 3TA, United Kingdom; [c]Department of Biochemistry, University of Oxford, Oxford OX1 3QU, United Kingdom; [d]Department of Physiology Anatomy and Genetics, University of Oxford, Oxford OX1 3PT, United Kingdom; and [e]School of Life Sciences & Department of Chemistry, University of Warwick, Coventry CV4 7AL, United Kingdom

TMEM16A Ca^{2+}-activated chloride channels are involved in multiple cellular functions and are proposed targets for diseases such as hypertension, stroke, and cystic fibrosis. This therapeutic endeavor, however, suffers from paucity of selective and potent modulators. Here, exploiting a synthetic small molecule with a biphasic effect on the TMEM16A channel, anthracene-9-carboxylic acid (A9C), we shed light on sites of the channel amenable for pharmacological intervention. Mutant channels with the intracellular gate constitutively open were generated. These channels were entirely insensitive to extracellular A9C when intracellular Ca^{2+} was omitted. However, when physiological Ca^{2+} levels were reestablished, the mutants regained sensitivity to A9C. Thus, intracellular Ca^{2+} is mandatory for the channel response to an extracellular modulator. The underlying mechanism is a conformational change in the outer pore that enables A9C to enter the pore to reach its binding site. The explanation of this structural rearrangement highlights a critical site for pharmacological intervention and reveals an aspect of Ca^{2+} gating in the TMEM16A channel.

TMEM16A | calcium signalling | pharmacology | CaCC

The calcium-activated chloride channel (CaCC) coded by the *TMEM16A* gene (HUGO gene nomenclature: *Anoctamin-1*) is expressed in a variety of cell types and is involved in vital functions including the control of smooth muscle tone, epithelial ion transport, and cell proliferation (1). TMEM16A channels are typically activated by agonist-induced Ca^{2+} release as a consequence of G_q protein-coupled receptor activation. Therefore, TMEM16A channels couple changes in intracellular Ca^{2+} concentration to cell electrical activity. TMEM16A is the founding member of a family composed of 10 proteins (TMEM16x) with different function. Some TMEM16x proteins operate as CaCCs (TMEM16A and TMEM16B) (2) while others work as lipid scramblases (e.g., TMEM16K) (3) or have a combined channel and scramblase function (e.g., TMEM16E and TMEM16F) (4, 5).

TMEM16A channels have been proposed as novel therapeutic drug targets. TMEM16A activators could constitute new treatments for conditions such as cystic fibrosis or chronic obstructive pulmonary disease, while inhibitors may be exploited in the treatment of problems such as hypertension and stroke (1, 6, 7). As TMEM16A is up-regulated in cancer and has a role in the control of cell proliferation, TMEM16A inhibitors may also have implications for cancer therapy (8, 9). Since the cloning of the TMEM16A channel, several small molecule modulators have been generated, including 2-(4-chloro-2-methylphenoxy)-N-[(2-methoxyphenyl)methylideneamino]-acetamide (Ani9) (10) and N-((4-methoxy)-2-naphthyl)-5-nitroanthranilic acid (MONNA) (11). These molecules inhibit the channel at submicromolar concentrations. Activators (such as (3,4,5-Trimethoxy-N-(2-methoxyethyl)-N-(4-phenyl-2-thiazolyl)-benzamide) (E_{act})) potentiate CaCC currents in airway epithelial cell lines (12), but whether E_{act} acts directly on TMEM16A has been questioned (13). There is significant ongoing effort toward the identification of novel TMEM16A inhibitors and activators (14–16). The mechanisms of action and binding sites of these small molecules, however, remain undefined. Some modulators, such as anthracene-9-carboxylic acid (A9C), display a biphasic effect on the TMEM16A channel when applied to the extracellular side of the membrane. Specifically, A9C inhibits the channel by acting as a pore blocker and also allosterically activates the channel by enhancing the channel sensitivity to Ca^{2+} and voltage (V_m) (thus also acting as a "potentiator") (17). These effects require the binding of A9C to site(s) within the pore of the TMEM16A channel (17). Endogenous ligands such as intracellular Ca^{2+} and plasmalemmal phosphatidylinositol 4,5-bisphospate (PIP_2) also modulate TMEM16A gating (18, 19). Thus, fundamental and structural knowledge underpinning channel-gating is required to shed light on the mechanisms of ligand (endogenous or synthetic) modulation of TMEM16A channel activity.

The TMEM16A channel is a homodimer encompassing two pores that function independently (20, 21). Each monomer contains two high-affinity Ca^{2+}-binding sites that couple ion-binding to channel-opening (22, 23). Each pore possesses a steric gate constituted by an intracellular portion of the sixth transmembrane helix (TM6). A hinge point formed by glycine at position 640 is involved in the conformational change of this intracellular-facing gate in response to Ca^{2+}-binding (22, 24) (Fig. 1*A*). Alanine

Significance

The TMEM16A calcium-gated chloride channels participate in a range of vital physiological functions. TMEM16A channels are desirable new drug targets as their dysfunction can lead to pathology. In spite of this, their pharmacology is still in its infancy. Gaining insight into the mode of action and binding sites for test compounds forms the basis for the development of new TMEM16A-interacting drugs. Here, we demonstrate that intracellular calcium triggers a conformational change in the outer mouth of the channel, which enables entry of a small molecule into the pore. Characterization of this structural rearrangement defines a critical site for pharmacological intervention and reveals an aspect of calcium gating in the TMEM16A channel.

PHARMACOLOGY

substitution of neighboring amino acids, such as isoleucine and glutamine at position 637 and 645 (I637A and Q645A), stabilizes the TM6 in the open state and results in channels that are open in the absence of intracellular Ca^{2+} and at positive V_m (here referred to as "constitutively open") (24, 25) (Fig. 1 *B* and *C*). A second gating mechanism is constituted by the Ca^{2+}-binding sites which encompass a series of negatively charged residues (25). The vacant Ca^{2+}-binding sites form an electrostatic barrier to anion permeation (defined as the "electrostatic gate"). This electrostatic barrier is removed upon Ca^{2+}-binding due to attenuation of the negative charge density of the Ca^{2+}-binding pocket (25).

The TMEM16 scramblases such as TMEM16K and the *Aspergillus fumigatus* TMEM16 (afTMEM16) have been structurally shown to rearrange at the outer region of the pore to permit lipid scrambling in response to Ca^{2+}-binding (3, 26). Understanding whether analogous gating rearrangements in the outer pore take place in TMEM16A is an important standing question in the field, since this may affect the action of small molecules acting from the extracellular side of the membrane.

Here, we set out to gain mechanistic insights into the action of A9C, a modulator of TMEM16A channel activity that acts exclusively when applied on the outer side of the membrane (17). We found that mutant channels in which the TM6 steric gate is stabilized in the open state in the absence of intracellular Ca^{2+} were entirely insensitive to extracellular A9C. However, when intracellular Ca^{2+} was present, these mutant channels regained sensitivity to extracellular A9C, revealing the unexpected finding that intracellular Ca^{2+} is mandatory for the action of an extracellular modulator. We provide evidence that Ca^{2+} allows the action of A9C on the channel by triggering a conformational change in the outer pore that enables A9C binding/efficacy. Our work may have significant implications for future drug design as it highlights the outer mouth of the channel as a site for pharmacological intervention.

Results

Ca^{2+} Sensitivity of Constitutively Active TMEM16A Mutant Channels.
A9C acts as an open-channel blocker and allosteric activator of the

channel sensitivity to intracellular Ca^{2+} at a given V_m (17). We generated mutant channels that show activity in the absence of intracellular Ca^{2+}, termed TMEM16A-Q645A and TMEM16A-I637A. The mutations bias the steric gate (constituted by TM6) of the channel toward the open conformation (24, 25). This enables the study of the effect of A9C on channels with the steric gate open.

During inside-out patch-clamp recordings at a constant positive V_m (+70 mV), wild-type TMEM16A channels were inactive in Ca^{2+}-free intracellular solution, and the current progressively increased as the intracellular Ca^{2+} concentration ($[Ca^{2+}]_i$) was raised up to $\sim$80 µM (Fig. 1*D*). The relationship between $[Ca^{2+}]_i$ and the TMEM16A current was fitted with *SI Appendix*, Eq. **S1** with half-maximal effective concentration (EC_{50}) of 0.7 µM (Fig. 1*D* and *SI Appendix*, Table S1). In contrast, both TMEM16A-Q645A and -I637A channels mediated a significant basal current in 0 $[Ca^{2+}]_i$ (Fig. 1*D*). When the patch was exposed to $[Ca^{2+}]_i$ ranging from $\sim$0.05 to $\sim$80 µM, an additional current increase was observed (Fig. 1*D*). The $[Ca^{2+}]_i$-response curves for TMEM16A-Q645A and -I637A were characterized by EC_{50} of 0.22 µM and 0.19 µM, respectively (*SI Appendix*, Table S1). We hypothesized that Ca^{2+} activation of TMEM16A-Q645A and -I637A channels may be due to either 1) disinhibition of the electrostatic gate and/or 2) gating-associated conformational changes triggered by Ca^{2+}.

Whole-Cell Current Magnitude and Kinetics of Wild-Type and Mutant TMEM16A Channels.
To examine whether Q645A and I637A mutations alter the channel response to the V_m, whole-cell currents were recorded in response to a "IV" protocol (*SI Appendix, Supplementary Information Text*). In the absence of Ca^{2+}, the currents recorded from cells transfected with TMEM16A were indistinguishable from the very-small currents observed from mock-transfected cells (2, 25). In the presence of 0.3 µM $[Ca^{2+}]_i$, hyperpolarizing and depolarizing steps showed instantaneous TMEM16A currents followed by time-dependent relaxations toward new steady-state levels. For wild-type TMEM16A channels, we observed a nearly linear relationship between the instantaneous current (measured at the start of the pulse) and V_m (*SI Appendix*,
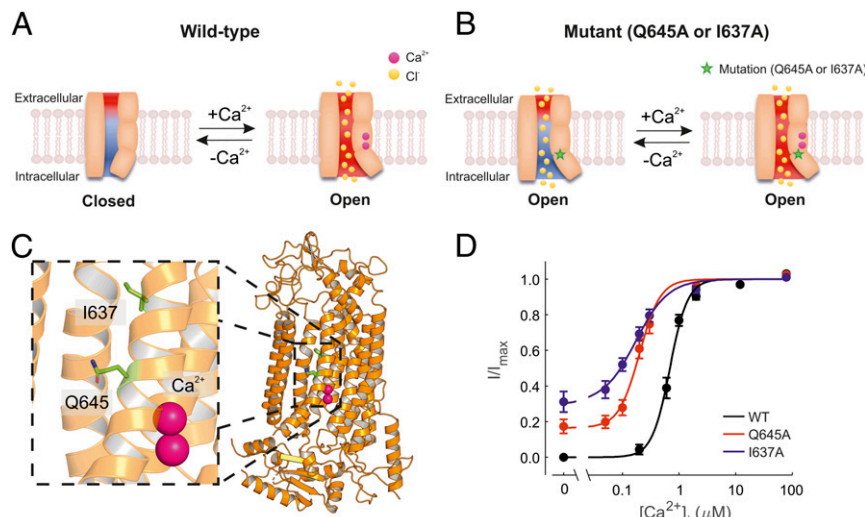
Fig. 1. Ca^{2+} sensitivity of TMEM16A, TMEM16A-Q645A, and -I637A channels. (*A*) Diagrammatic representation of the TMEM16A channel pore and associated gating mechanisms based on previously published work (22, 24, 25, 31). The movement of the TM6 helix during gating is represented as a tilt on one side of the pore as the result of Ca^{2+} binding. The red and blue backgrounds depict negative and positive electrostatic potentials in the pore, respectively. The electrostatic gate is attenuated upon Ca^{2+} binding. (*B*) Diagrammatic representation of constitutively open channels (TMEM16A-Q645A and -I637A). The term "constitutively open" is used here to denote channels that are open in the absence of intracellular Ca^{2+} at positive V_m. Mutations are indicated by the star symbol. In these mutant channels, the electrostatic gate is presumably intact and can be attenuated upon Ca^{2+} binding. (*C*) The cryo-EM structure of TMEM16A with bound Ca^{2+} shown in pink (PDB ID: 5OYB). (*D*) Mean relationships between $[Ca^{2+}]_i$ and the current measured at +70 mV for TMEM16A (*n* = 10), TMEM16A-Q645A (*n* = 7), and -I637A (*n* = 7), as indicated. The smooth curves are best fits of *SI Appendix*, Eq. **S1** to the data.

www.manaraa.com

Fig. S1*B, i*). However, the relationship between steady-state current and the V_m was outwardly rectifying (*SI Appendix,* Fig. S1*B, ii*). This phenomenon was expressed as the ratio between the steady-state and instantaneous current at +100 mV (I_{ss}/I_{inst}) (*SI Appendix,* Table S2). The extent of outward rectification was quantified as the ratio between the steady-state current measured at +100 mV (I_{100}) and −100 mV (I_{-100}). The I_{100}/I_{-100} (rectification index) was −29 for the wild-type TMEM16A channel in 0.3 μM $[Ca^{2+}]_i$ (*SI Appendix,* Table S2). The time course of the V_m-dependent current increase was calculated as the time required to reach the half-maximal current ($\tau_{0.5}$) at the different V_m (*SI Appendix,* Fig. S1*B, ii, Inset*).

Consistent with the measurement in inside-out patches described above (Fig. 1*D*), significant currents were detected in 0 $[Ca^{2+}]_i$ in whole-cell recordings from cells expressing TMEM16A-Q645A and -I637A channels. These currents were activated almost instantaneously without the slow time-dependent activation observed for wild-type channels. Thus, the instantaneous and the steady-state currents essentially coincided (*SI Appendix,* Fig. S1 *C, i* and *D, i*); the I_{ss}/I_{inst} was 1.2 for TMEM16A-Q645A and -I637A channels (*SI Appendix,* Table S2). The $\tau_{0.5}$ was difficult to quantify since the small time-dependent current activation occurred in less than ∼10 ms.

To achieve a level of activation above the baseline in the mutants comparable to the wild-type channels in 0.3 μM $[Ca^{2+}]_i$, we buffered $[Ca^{2+}]_i$ to 0.1 μM in the whole-cell TMEM16A-Q645A and -I637A currents recording. Under these conditions, in response to depolarizing pulses, the mutants showed a slow time-dependent activation similar to that observed for wild-type channels (*SI Appendix,* Fig. S1 *C, ii* and *D, ii*). The I_{ss}/I_{inst} was 1.9 and 3.6, and the rectification index I_{100}/I_{-100} was −27 for TMEM16A-Q645A and -I637A currents, respectively (*SI Appendix,* Table S2).

Effect of A9C on Wild-Type and Mutant TMEM16A Channels in the Absence or Presence of Ca²⁺. We next studied the effect of extracellular A9C on wild-type and mutant channels. A concentration of A9C (300 μM) close to the reported half-maximal inhibitory concentration (IC_{50}) (17) was used. Whole-cell currents were elicited in response to the "IV tail" protocol (*SI Appendix, Supplementary Information Text*). Extracellular A9C induced complex changes in the whole-cell TMEM16A current (Fig. 2*A*) (17). The current measured at the beginning of the tail pulse was significantly potentiated in the presence of A9C (by approximately sevenfold at −100 mV) (Fig. 2 *B, i*). In contrast, the current measured at the end of the tail pulse (steady-state) was inhibited at positive V_m (by approximately threefold at +140 mV) (Fig. 2 *B, ii*). To our surprise, the TMEM16A-Q645A and -I637A currents recorded in 0 $[Ca^{2+}]_i$ were entirely insensitive to extracellular A9C at all V_m tested. These channels remained insensitive to A9C even at much higher concentrations (*SI Appendix,* Fig. S2). We also examined the effect of A9C on the mutant channels in the presence of 0.1 μM $[Ca^{2+}]_i$. Strikingly, intracellular Ca²⁺ conferred the channels the ability to respond to A9C in a manner quantitatively similar to that observed for the wild-type channels (Fig. 2*B* and *SI Appendix,* Fig. S2). For example, the TMEM16A-Q645A and -I637A currents were activated by approximately five- and threefold at −100 mV and inhibited by approximately two- and fivefold at +140 mV, respectively. For both wild-type and mutant channels, A9C did not profoundly affect the E_{rev}, which was very close to the expected equilibrium potential for Cl⁻ (E_{Cl}) in our recording conditions (∼0 mV) in each case (Fig. 2 *B, i*). Collectively, this set of experiments demonstrated that intracellular Ca²⁺ is a key regulator of the response of the TMEM16A channel to A9C, an extracellular-acting synthetic small molecule.

Separation of the Inhibitory and Activating Effects of A9C on the TMEM16A Channel during Concentration Jump Experiments. To separate the inhibitory and activating effects of A9C on wild-type

and mutant TMEM16A channels, whole-cell currents were measured at +70 mV in the absence or presence of $[Ca^{2+}]_i$ while A9C (300 μM) was rapidly applied to the cell ("concentration jump"), as detailed in *SI Appendix*.
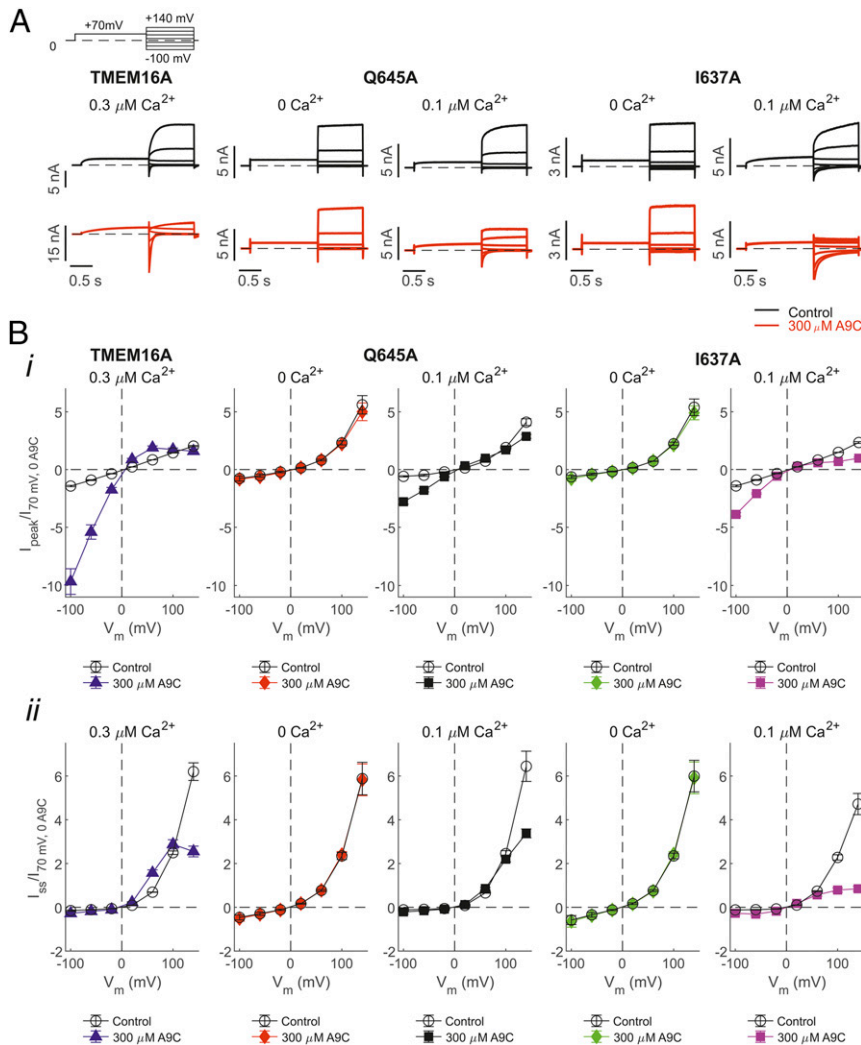
In 0 $[Ca^{2+}]_i$, wild-type TMEM16A channels were closed, and extracellular A9C did not increase the current amplitude (Fig. 3*A*) (17); the ratio between the current measured in the presence (I_{A9C}) or absence (I_0) of A9C was 1.06 ± 0.05 ($n = 5$). In 0 $[Ca^{2+}]_i$, the TMEM16A-Q645A or -I637A currents were also unaffected by extracellular A9C (300 μM) (Fig. 3*A*), and the I_{A9C}/I_0 was 1.01 ± 0.01 ($n = 5$, Q645A) and 0.99 ± 0.01 ($n = 5$, I637A). In the presence of 0.3 μM $[Ca^{2+}]_i$, when A9C was rapidly applied to the bath solution, the TMEM16A current amplitude quickly declined before increasing to a new steady-state level (Fig. 3*A*). As A9C was removed, a dramatic increase in the current was observed followed by a return of the current to the level measured in the absence of A9C (Fig. 3*A*). A similar complex response was observed when A9C was applied to cells expressing TMEM16A-Q645A or -I637A channels and in the presence of 0.1 μM $[Ca^{2+}]_i$. These phenomena were interpreted as the combination of an inhibiting (block) and activating effect of A9C on TMEM16A channels. The initial decline in current at the start of the concentration jump presumably represents fast open-channel block by A9C, and the subsequent current potentiation is probably caused by a slower allosteric effect on channel-gating caused by A9C binding (17). The rapid washout of A9C produced a fast relief of channel block, while an allosteric activating effect appeared to persist (17). Consistent with this proposition, when $[Ca^{2+}]_i$ was elevated to maximally activate the channel, A9C only blocked the channel (*SI Appendix,* Fig. S3), because the high open probability triggered by high $[Ca^{2+}]_i$ leaves limited scope for further activation.

In the presence of submaximal $[Ca^{2+}]_i$, the inhibitory effect of A9C was estimated by back extrapolating the current amplitude (I_b) to the point when the drug was added. The current activation (I_a) was quantified via back extrapolation of the transient spike of the current observed upon drug washout (*SI Appendix, Supplementary Information Text*). The extent of blockage was expressed as I_b/I_0, and the extent of current activation was expressed as I_a/I_0 (Fig. 3*C*). This analysis demonstrated that in the presence of $[Ca^{2+}]_i$, TMEM16A-Q645A was less sensitive to A9C inhibition and activation, consistent with our proposition that Q645 forms part of the A9C binding site (see below, *Identification of the A9C Putative Binding Site*). In contrast, TMEM16A-I637A channels have a similar sensitivity to A9C inhibition but reduced activation, possibly indicating a role for I637 in the mechanism of A9C activation. This is also manifested by the fact that the time course of wash-out of the A9C effect (Fig. 3*A*) was characterized by a different time constant of 0.29 ± 0.01 s ($n = 10$) and 1.93 ± 0.12 s ($n = 9$) for TMEM16A-Q645A and -I637A channels, respectively. I_{A9C}, the steady-state current measured during the application of A9C reflects the combined inhibitory and activating effects of A9C. The I_{A9C}/I_0 was 1.78 ± 0.18 ($n = 6$), 1.09 ± 0.07 ($n = 10$), and 0.60 ± 0.07 ($n = 9$) for TMEM16A, TMEM16A-Q645A, and -I637A channels, respectively.

In summary, the data described above indicated that intracellular Ca²⁺ serves as "switch" to enable the action of A9C on the channel. The experiments described below aimed to test the mechanism(s) by which intracellular Ca²⁺ enables the action of extracellular A9C.

Assessing the Influence of the Electrostatic Gate on the Effect of A9C. The vacant Ca²⁺-binding sites form an electrostatic gate for the permeating ion (25). We hypothesized that in the absence of Ca²⁺, the unoccupied Ca²⁺ binding pocket, which is characterized by negatively charged residues (such as E650), might electrostatically repel the carboxylate group on the A9C molecule. To test this possibility, we mutated, in the background of the Q645A (steric gate) mutation, E650 into alanine or arginine,

Dinsdale et al.
An outer-pore gate modulates the pharmacology of the TMEM16A channel

www.manaraa.com

Fig. 2. Effects of extracellular A9C on whole-cell TMEM16A, TMEM16A-Q645A, and -I637A currents in the absence or presence of intracellular Ca^{2+}. (*A*) Whole-cell currents recorded from HEK-293T cells expressing TMEM16A, TMEM16A-Q645A, or -I637A channels in the absence (control) or presence of 300 μM $[A9C]_{ext}$ and the indicated $[Ca^{2+}]_i$. The stimulation protocol is shown in the *Upper Left*. Dashed horizontal lines represent the zero-current level. (*B*) Mean-peak (*i*) or steady-state (*ii*) whole-cell current density versus V_m relationships measured in the absence or presence of 300 μM $[A9C]_{ext}$ and various $[Ca^{2+}]_i$, for the various channel types, as indicated. The number of experiments was 6 to 10 in each case.

since this is expected to reduce Ca^{2+} binding and thus also impact the extent of attenuation of the electrostatic gate by Ca^{2+} (25, 27) (Fig. 4*A*).

We tested the Ca^{2+} sensitivity of TMEM16A-Q645A-E650A and -Q645A-E650R channels using inside-out recordings (Fig. 4*B*). The double mutants were constitutively active in 0 $[Ca^{2+}]_i$ (Fig. 4*B*). The increase of $[Ca^{2+}]_i$ caused additional activation of TMEM16A-Q645A-E650A and -Q645A-E650R currents; the current versus $[Ca^{2+}]_i$ relationships were respectively characterized by an EC_{50} of 0.63 μM ($n = 9$) and of 0.93 μM ($n = 9$) (*SI Appendix,* Table S1). This is consistent with the fact that mutations in E650 reduced the extent of Ca^{2+} binding (24, 25). In 0 $[Ca^{2+}]_i$, whole-cell TMEM16A-Q645A-E650A and -Q645A-E650R currents in response to the "IV tail" protocol were unaffected by application of extracellular A9C (300 μM) at any V_m tested (Fig. 4*C*).

The disengagement of the electrostatic gate is manifested by loss of rectification (25). When the inside-out patches expressing TMEM16A-Q645A-E650A or -Q645A-E650R were exposed to increasing $[Ca^{2+}]_i$, the current amplitude increased, especially at positive V_m (Fig. 4 *D, i*). Fig. 4*D* shows that despite the current increase, there were modest changes in the extent of rectification,

suggesting that the electrostatic gate was only partially disengaged, presumably because the E650A/R mutation reduced binding of Ca^{2+} to one of the two sites. In contrast, exposure of the intracellular side of the patch to 5 mM Gd^{3+} ($[Gd^{3+}]_i$) led to a nearly linear current–voltage relationship, consistent with a more substantial attenuation of the electrostatic gate caused by this trivalent cation (Fig. 4*D*) (25). In fast perfusion experiments, the extent of (extracellular) A9C inhibition in the presence of Gd^{3+} was ~20% and 5% for TMEM16A-Q645A-E650A and -Q645A-E650R channels, respectively (Fig. 4*E*). However, in presence of high (~12 or 200 μM) $[Ca^{2+}]_i$, which caused a lesser degree of attenuation of the electrostatic gate (Fig. 4*D*), extracellular A9C caused ~40% inhibition of TMEM16A-Q645A-E650A and - Q645A-E650R currents (Fig. 4*E*). Collectively, these data suggest that the electrostatic gate has a moderate influence on the action of A9C and that the effect of Ca^{2+} on the action of A9C may be secondary to Ca^{2+}-induced gating rearrangement of the outer pore.

Assessing the Effect of Ca^{2+} on Cl^- Permeation: Evidence for a Structural Rearrangement of the Outer Pore Region. To probe for potential Ca^{2+}-mediated structural rearrangements in the outer

www.manaraa.com
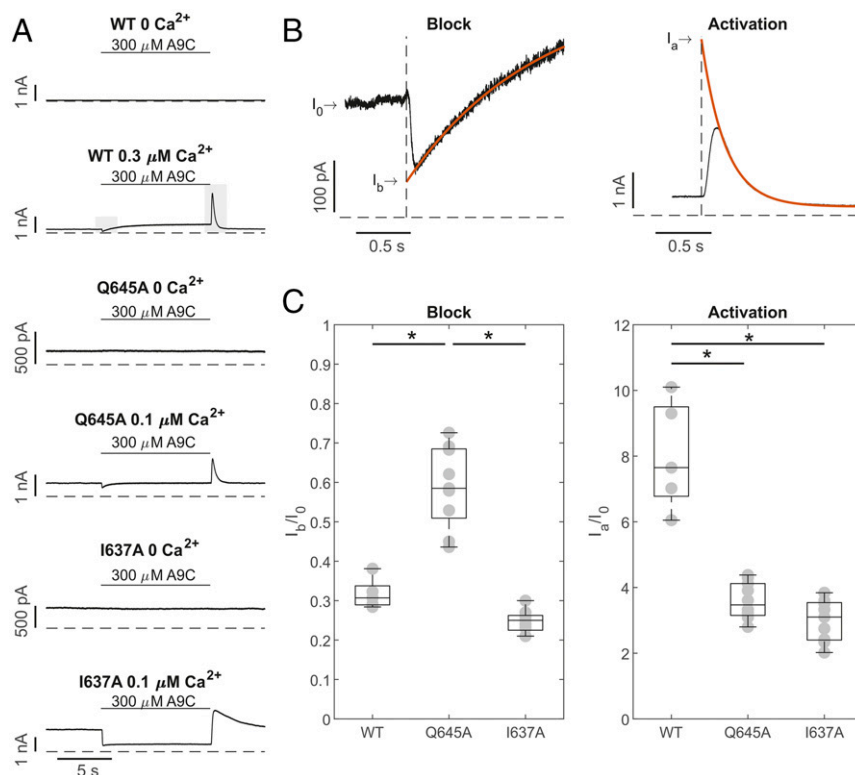
Fig. 3. Separation of inhibiting and activating effects of A9C on TMEM16, TMEM16A-Q645A, and -I637A channels. (*A*) Whole-cell currents recorded from HEK-293T cells expressing TMEM16A, TMEM16A-Q645A, or -I637A channels, as indicated. V_m was +70 mV, and $[Ca^{2+}]_i$ was 0, 0.1, or 0.3 μM, as indicated. Extracellular A9C (300 μM) was applied ("concentration jump") as indicated by the horizontal bars. Dashed horizontal lines represent the zero-current level. The shaded gray bars indicate regions of the recording that were expanded in *B*. (*B*) The continuous red traces represent single exponential fits used to back-extrapolate the currents to obtain I_b (*Left*) and I_a (*Right*). (*C*) Mean current inhibition (I_b/I_0, *Left*) and activation (I_a/I_0, *Right*) plotted for each channel type in box plots, as indicated. The number of experiments was 6 to 10 in each case. *$P < 0.05$, compared to TMEM16A.
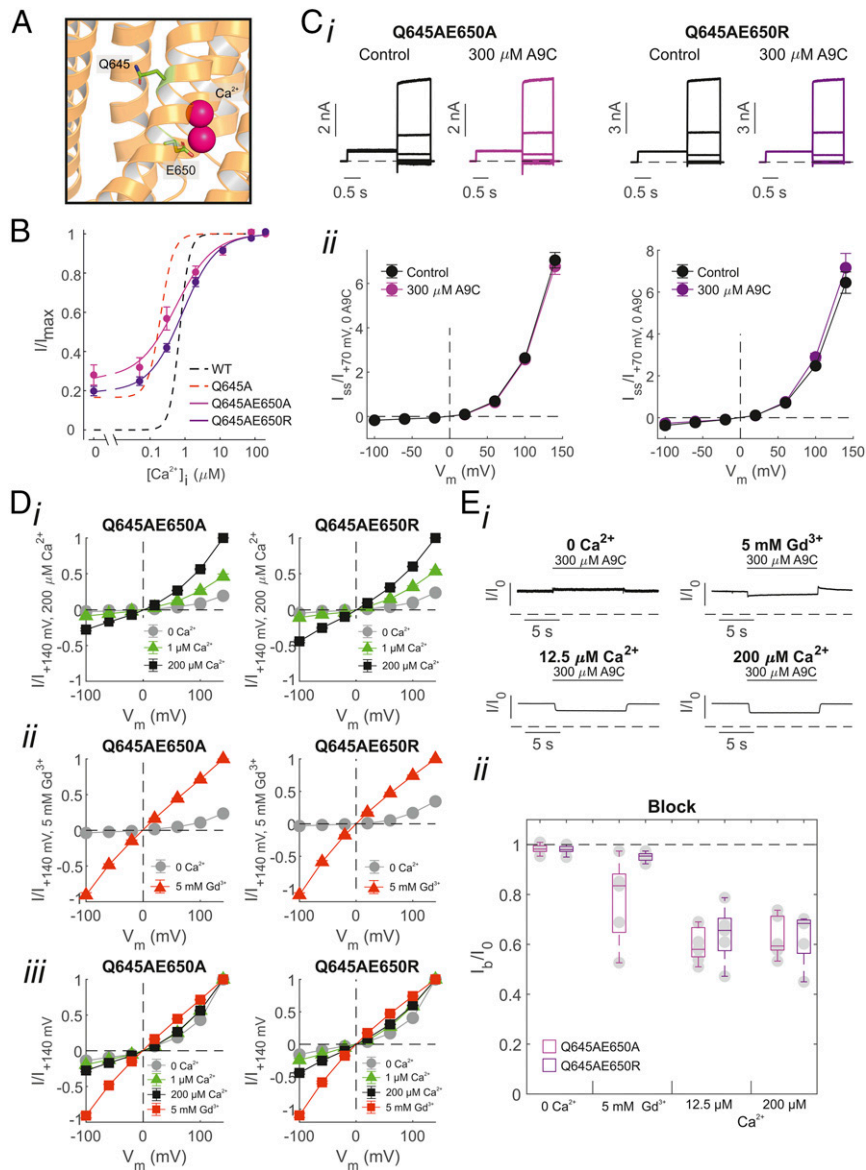
pore, we assessed the apparent affinity of Cl⁻ for the binding site(s) within the pore of the TMEM16A-Q645A channel in the absence or presence of intracellular Ca^{2+} and extracellular A9C. In these experiments, intracellular Cl⁻ was replaced with methanesulphonate, and strongly depolarizing V_m was used to favor unidirectional inward Cl⁻ fluxes through the pore during whole-cell recordings. The current was measured in the presence of varying concentrations of extracellular Cl⁻ ($[Cl^-]_o$). This allowed us to assess the relationship between the current amplitude and $[Cl^-]_o$ at various V_m (Fig. 5 *A* and *B*). The relationship between the apparent dissociation constant for Cl⁻ ($K_{0.5}$) obtained from the Hill fit (*SI Appendix*, Eq. **S5**) of these relationships and the V_m is shown in Fig. 5*C*.

To investigate the cross-influence of Ca^{2+} and A9C, we considered the thermodynamic cycle shown in Fig. 5*E* and calculated the coupling coefficient, Ω, as detailed in *SI Appendix, Supplementary Information Text*. Ω was greater than 1 at each V_m (Fig. 5*D*), which indicated that Ca^{2+} and A9C synergistically modulate Cl⁻ fluxes. This corresponds to a negative $\Delta\Delta G_{int}$ spanning from ~−0.4 kcal/mol (at +70 mV) to −1 kcal/mol (at +140 mV). Collectively, these results indicate that A9C and Ca^{2+} are strongly coupled in their effect on Cl⁻ transport in the TMEM16A channel. These results suggest that the effect of A9C on the channel is secondary to a Ca^{2+}-dependent gating rearrangement of the outer pore. This effect becomes more pronounced as the V_m is increased, presumably because membrane depolarization favors both 1) binding of intracellular Ca^{2+} and 2) entry of the negatively charged extracellular A9C into the pore.

Molecular Dynamics Simulations Offer Insight into the Structural Rearrangement of the Outer Pore Region. We used molecular modeling and molecular dynamics (MD) simulations to gain insights

into the Ca^{2+}-dependent conformational rearrangements of the outer pore. As there is not yet an experimentally determined structure of a fully open state of TMEM16A, we used the structure of TMEM16K (Protein Data Bank (PDB) entry: 5OC9) (3) and Ca^{2+}-bound TMEM16A (5OYB) (22) to build a model of TMEM16A in an open conformation. These structures mainly differ in the position of the TM4 helix. We therefore modeled the coordinates of TM4 from TMEM16K within the Ca^{2+}-bound TMEM16A structure.

SI Appendix, Fig. S4 provides a structural alignment of our open-state TMEM16A model with the deposited TMEM16x structures and the recently developed model of the PIP₂-bound open TMEM16A channel (28). The analysis demonstrates that our model closely resembled these structures and almost completely overlapped with the PIP₂-bound open TMEM16A channel model (28) with C_α RMSD of 1.8 Å (*SI Appendix*, Fig. S4 *E* and *F*). Our open-state model also showed comparable stability with the TMEM16A wild-type structures and PIP₂-bound model over three 200-ns simulations (*SI Appendix*, Fig. S4G). To test whether our model was conductive to solvent, we calculated the occupancy of the water molecules within the pore in the last 100 ns of the 800-ns simulation trajectory (Fig. 6*A* and Movie S1). The open-state model showed water molecules within the outer pore region. These simulations also reveal Cl⁻ binding at K584 and K641 and permeation of Cl⁻ within the pore (*SI Appendix*, Fig. S5), consistent with published experimental studies demonstrating that K641 serves as Cl⁻ binding site (29, 30). We studied the effect of Ca^{2+} on the open pore in 800-ns simulations ($n = 3$); as Ca^{2+} was removed, the pore narrowed, especially in proximity of V539 (TM4) and I636 (TM6) (Fig. 6 and Movie S2). These residues are in the vicinity of a gate (I637, I546, and I547 in the *a* TMEM16A

Dinsdale et al.
An outer-pore gate modulates the pharmacology of the TMEM16A channel

PNAS | 5 of 10
https://doi.org/10.1073/pnas.2023572118

www.manaraa.com

Fig. 4. Assessment of the contribution of the electrostatic gate on the effect of extracellular A9C on the TMEM16A channel. (*A*) The cryo-EM structure of TMEM16A with Q645 and E650 highlighted and bound Ca^{2+} shown in pink (PDB ID: 5OYB). (*B*) Mean relationships between $[Ca^{2+}]_i$ and the current measured at +70 mV in inside-out patches expressing TMEM16A-Q645A-E650A ($n = 9$) or -Q645A-E650R channels ($n = 9$). Dashed black and red lines are mean relationships between $[Ca^{2+}]_i$ and the current measured at +70 mV for TMEM16A and TMEM16A-Q645A, respectively, and are replotted from Fig. 1. (*C*) (*i*) Whole-cell TMEM16A-Q645A-E650A/R currents recorded in response to the "IV tail" protocol. $[Ca^{2+}]_i$ was 0. (*ii*) Mean whole-cell TMEM16A-Q645A-E650A or -Q645A-E650R current versus V_m relationships measured in the absence or presence of 300 μM [A9C]. The number of experiments was 6 to 8 in each case. (*D*) Mean current versus V_m relationships obtained in inside-out patches expressing TMEM16A-Q645A-E650A/R in the presence of (*i*) various $[Ca^{2+}]_i$ or (*ii*) 5 mM $[Gd^{3+}]_i$, as indicated. Currents were normalized for the current measured at +140 mV in (*i*) 200 μM $[Ca^{2+}]_i$ or (*ii*) 5 mM $[Gd^{3+}]_i$. (*iii*) Mean TMEM16A-Q645A-E650A/R currents versus V_m relationships normalized for the current measured at +140 mV in each case. The number of experiments was 6 to 8 in each case. (*E*) (*i*) Whole-cell TMEM16A-Q645A-E650A currents measured at +70 mV and in the presence of 0, 12, 200 μM $[Ca^{2+}]_i$, or 5 mM $[Gd^{3+}]_i$, as indicated. Extracellular A9C (300 μM) was applied ("concentration jump") as indicated by the horizontal bar. (*ii*) Mean current inhibition (I_b/I_0) plotted as box plot for each channel type. The number of experiments was 5 to 7 in each case. Dashed horizontal lines in C*i* and E*i* indicate the zero-current level.

variant) proposed in recent studies from the Dutzler group (31, 32). This suggests that by removing the Ca^{2+} from its binding site, the conformation of the outer pore converges toward the closed-state Ca^{2+}-free structure (5OYG) (22). These conformational rearrangements appear also in three 500-ns simulations of both TMEM16A-Q645A and -I637A (*SI Appendix, Fig. S6 A and B*). Collectively, our simulations indicate that Ca^{2+} ions are required to retain stable opening of the outer pore of the TMEM16A channel.

In addition to a closure of the outer pore without Ca^{2+}, we observed a kink in the TM6 helix, near the Ca^{2+}-binding site, equivalent

to that observed in the cryo-electron microscopy (cryo-EM) structures without Ca^{2+} (*SI Appendix, Fig. S6C* and Movie S2). In comparison with the wild-type open-state model, 500-ns simulations ($n = 3$) of the TMEM16A-Q645A and -I637A channels did not demonstrate the same degree of TM helix kinking in the absence of Ca^{2+}. This suggests that these mutations, at least partially, prevent the closure of the steric gate (TM6) of the channel (*SI Appendix, Fig. S6C*).

Identification of the A9C Putative Binding Site. We used AutoDock Vina to position A9C above the outer pore of the open-state

www.manaraa.com
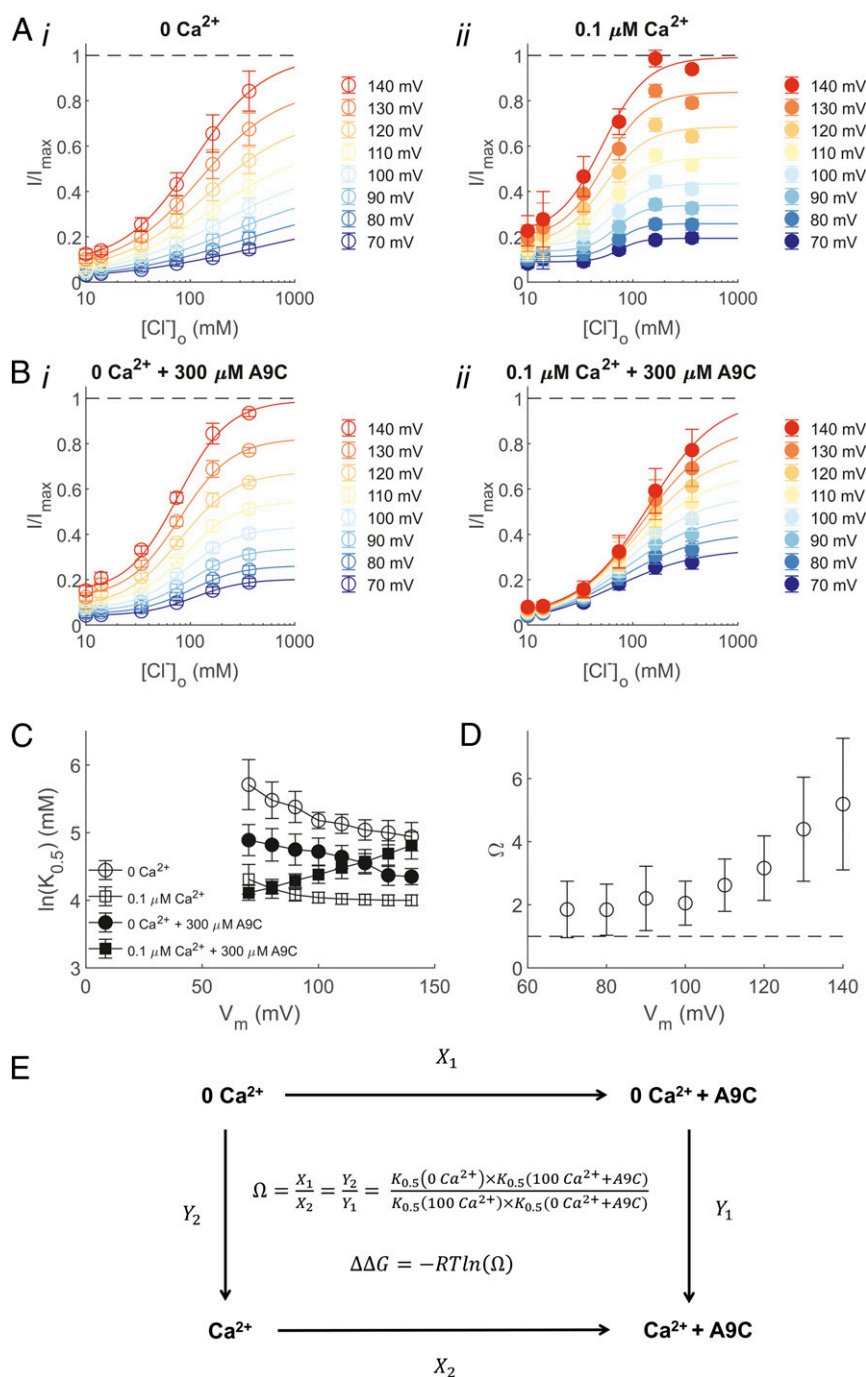
Fig. 5. Saturation and binding of Cl$^-$ within the TMEM16A-Q645A channel pore. (*A*) Mean relationships between [Cl$^-$]$_o$ and the TMEM16A-Q645A whole-cell current measured at various V_m in either (*i*) 0 or (*ii*) 0.1 μM [Ca^{2+}]$_i$, as indicated. The smooth curves are best fits of *SI Appendix*, Eq. **S5** to the data. The number of experiments was 7 in each case. (*B*) Mean relationships between [Cl$^-$]$_o$ and the whole-cell current measured at various V_m in either (*i*) 0 or (*ii*) 0.1 μM [Ca^{2+}]$_i$. The extracellular solution was supplemented with 300 μM A9C. The smooth curves are best fits of *SI Appendix*, Eq. **S5** to the data. The number of experiments was 8 to 9 in each case. (*C*) K$_{0.5}$ versus V_m relationships obtained in the absence or presence of intracellular Ca^{2+} and extracellular A9C, as indicated. The number of experiments was 7 to 9 in each case. (*D*) Calculated Ω plotted versus V_m. (*E*) Thermodynamic cycle illustrating the interactions between Ca^{2+} and A9C.

TMEM16A model. In the presence of Ca^{2+}, A9C translocated from the extracellular side of the membrane to its putative binding site in the first 100 ns and remained at this site for the entire duration (200 ns) of the simulation (Fig. 7*A*). In the simulation in which A9C was applied to the intracellular side, A9C did not penetrate into the pore. This finding is in agreement with our previous report (17) where we found that A9C was not able to act from the cytosolic side of the channel during patch-clamp experiments (*SI Appendix*, Fig. S7). In the absence of Ca^{2+}, pore closure at V539 and I636 prevented A9C from reaching the binding site (Fig. 7 *A* and *B*). Our simulations also demonstrated that A9C could not reach this binding site in any of the cryo-EM structures, which all have a closed outer pore (Fig. 7*C*). The residues forming the putative A9C-binding site
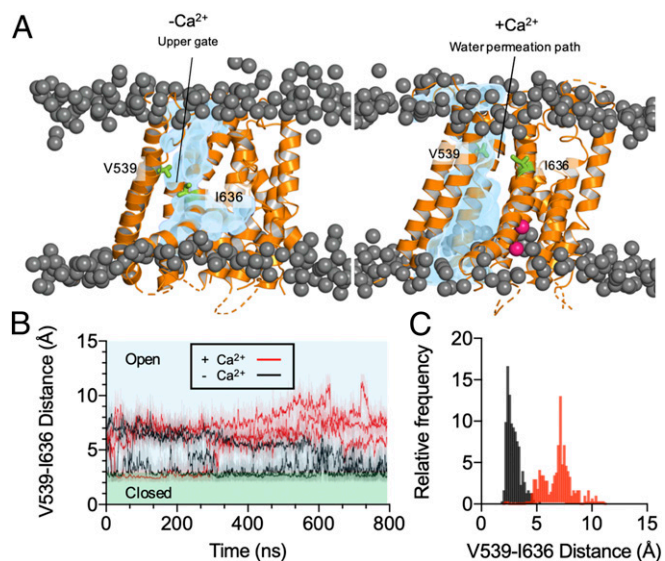
Fig. 6. Occupancy of water molecules inside the TMEM16A pore. (*A*) Representative calculations of the average occupancy of the water molecules inside the pore of the open TMEM16A channel over the last 100 ns of an 800-ns simulation with and without Ca^{2+}. The occupancy of the water molecules is shown in blue. The phosphate headgroups are shown as dark gray spheres. The protein is represented as cartoon in orange. V539 and I636 are shown in green. Ca^{2+} is shown in pink. (*B*) Calculated minimum distance between V539 and I636 in the Ca^{2+}-bound (red) and the Ca^{2+}-free (black) state across 800-ns simulations ($n = 3$). The lighter shaded lines show the distance calculated every 10 ps, and the darker lines show running averages over 1 ns. (*C*) Histogram showing V539-I636 distance in the last 100 ns of the simulations. The two conditions, Ca^{2+}-bound (red) and the Ca^{2+}-free (black) states, were sampled with the bin size of 0.17 Å and sampled every 1 ns ($n = 3$).

were identified as being within 4 Å from the A9C molecule for at least 50% of the last 100 ns of the simulation. These residues were: S513, V539, I636, K641, and Q645 (Fig. 7*D*). The same residues were identified when the simulation was performed on the PIP_2-bound TMEM16A open state structure (28) (*SI Appendix*, Fig. S8). The carboxyl group of A9C coordinated with K641, while its aromatic rings interacted with the hydrophobic side chains of I636 and V539 (Fig. 7 *A, Right*). Overall, our simulations suggested that a Ca^{2+}-dependent outer-pore rearrangement crucially enables A9C to reach its putative binding site, consistent with the electrophysiology data shown above.

We mutated the residues that form the putative binding site (S513, V539, I636, K641, and Q645) to alanine one at a time. The sensitivity of these mutant channels to A9C was tested using concentration jump experiments during whole-cell recordings. Fig. 7*E* shows that both the inhibitory (I_b/I_0) and activatory (I_a/I_0) effects of A9C were dramatically reduced for all mutant channels. The most significant inhibition was observed for the I636 mutant (Fig. 7*E*), which abolished the effects of A9C. The effect of A9C on the I636 mutant was therefore tested in a broader A9C concentration range. *SI Appendix*, Fig. S9 shows that the channel is virtually insensitive to A9C concentrations as high as 1 mM.

Discussion

Our key findings highlight the link between the action of intracellular Ca^{2+} and extracellular A9C on the TMEM16A channel. The underlying mechanism is a Ca^{2+}-triggered conformational change at the outer pore, which allows A9C to reach the center of the channel. Guided by the cryo-EM structures of the Ca^{2+}-bound TMEM16A and TMEM16K proteins, we generated an open-state

model of the TMEM16A channel. Using MD simulations, we identified a path for the A9C molecule to access its binding pocket inside the pore from the extracellular side of the channel. The A9C-binding pocket is partially hydrophobic and shares the same basic residue, K641, required for Cl^- coordination (29, 30). Our results highlight a potential druggable site at the outer pore of the channel and shed light on an aspect of Ca^{2+}-gating of the TMEM16A channel.

Gating Mechanisms of TMEM16 Channels and Scramblases. Like some other anion channels, such as mammalian CLC and prokaryotic FluC channels (33, 34), the TMEM16A channel is a homodimer encompassing two pores that function independently from one another (20, 21). Ca^{2+} binding to sites in each monomer triggers channel activation (22, 23) by promoting a hinging motion of TM6 which evoke opening of the "steric gate" at the intracellular pore (22, 24, 31, 32) (Fig. 1). In line with a recently published structural work (32), we note that in our simulations, the TMEM16A-Q645A and -I637A channels in the absence of Ca^{2+} have the TM6 helix in a pre-open intermediate state with potentially incomplete pore opening (*SI Appendix*, Fig. S4C). In these channels, intracellular Ca^{2+} triggers a conformational change in the outer pore. This conformational change enables A9C to reach its putative binding site.

Negatively charged residues at the Ca^{2+}-binding sites constitute an electrostatic gate/barrier, which is attenuated by Ca^{2+} occupancy (25). Here, we provide evidence of a previously anticipated gating component of the channel constituted by the hydrophobic residues between TM4 and TM6, in particular V539 and I636. Other hydrophobic residues on TM4 (such as I546 and I547) and TM6 (such as I637) have recently been demonstrated to form a gate (31, 32). The Ca^{2+}-dependent widening of the outer pore at V539 and I636 is similar to that seen in TMEM16 scramblases such as *Nectria haematococca* TMEM16 (nhTMEM16). Lipid transport in nhTMEM16 requires the opening of the outer region of the permeation pathway involving residues homologous to V539 and I636 in TMEM16A (nhTMEM16 T333 and Y439) (35, 36). Our data suggest that TMEM16x channels and scramblases may share a common Ca^{2+}-dependent mechanism that widens the outer pore. The notion that a single-point pore mutation confers scramblase activity on TMEM16A (37) is consistent with the idea that the lipid and ion permeation pathways in TMEM16x proteins may share a similar overall geometry.

Identification of a Putative Binding Site for A9C in the TMEM16A Channel. We showed that A9C penetrates the channel when the outer pore is open and reaches a region composed of five amino acids (S513, V539, I636, K641, and Q645). While separating the effects of mutations on gating and binding poses challenges (38), the combined use of electrophysiology and MD simulations suggests that this region is a binding site for A9C. This is consistent with our previous work in which we suggested that for wild-type TMEM16A channels, extracellular A9C competes with the permeating ion within the pore (17). A9C is a widely used tool compound in Cl^- channel research (17, 39). Our discovery of the A9C-binding region on the TMEM16A channel has significant implications for future drug discovery as it may constitute a possible site of action for synthetic modulators of the channel.

TMEM16A as a Therapeutic Drug Target. TMEM16A has been proposed as a drug target for a range of human pathologies. TMEM16A is a key depolarizing mechanism in arterial smooth muscle, and opening of TMEM16A results in arterial smooth-muscle contraction (40–44). TMEM16A activators/potentiators and blockers could be employed to treat diseases associated with altered arterial tone including orthostatic hypotension and (systemic and pulmonary) hypertension, respectively. TMEM16A is

www.manaraa.com
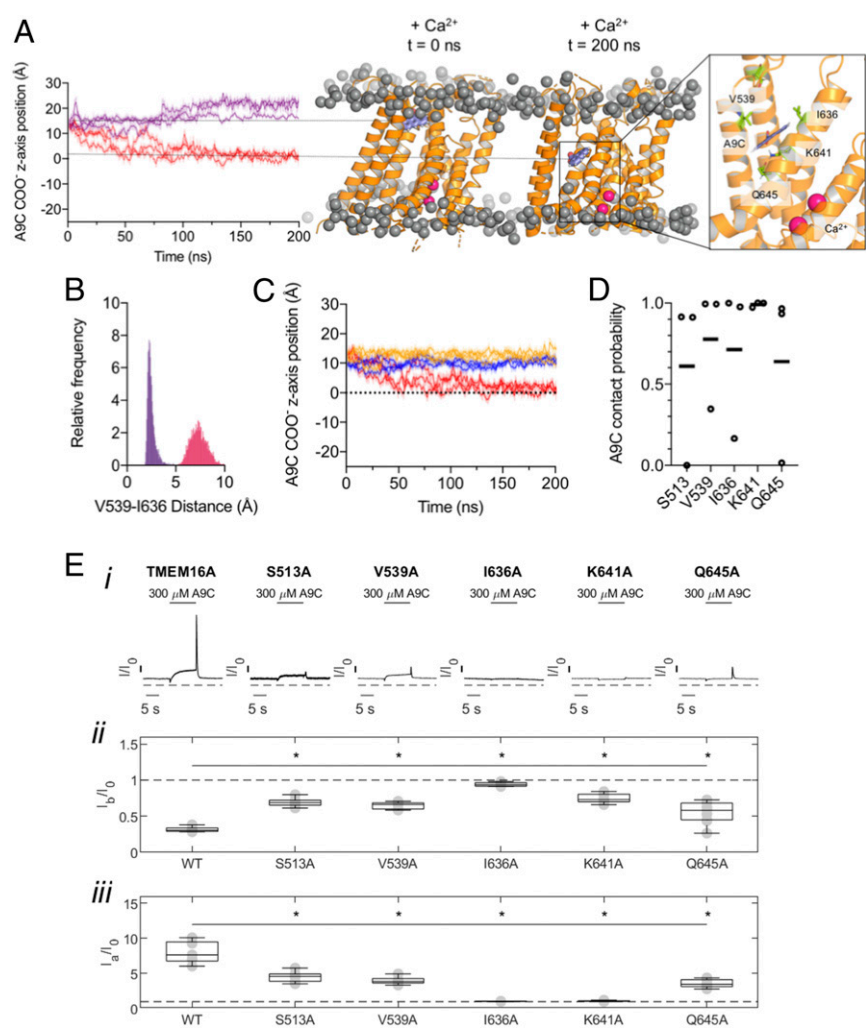
Fig. 7. Identification of the putative A9C binding site. (*A*) z-axis position of an A9C molecule within our open-state model (center of the bilayer set as 0). The positive and negative values define the movement of the A9C toward the extracellular or intracellular side of the pore, respectively. The simulations were run in the presence (red) or absence of Ca^{2+} (purple). The initial position of both simulations is marked with the top horizontal line. The bottom horizontal line shows position of the A9C binding site. For each trace, the distance calculated every 10 ps (shaded), and running averages over 1 ns are shown ($n = 3$). The *Right* shows A9C (blue) after 200 ns of simulation. The residues with a contact probability greater than 0.5 are shown in green. (*B*) Histogram (bin size: 0.05 Å) of V539-I636 distance in the Ca^{2+}-bound (red) and the Ca^{2+}-free (purple) state during the last 100 ns of the simulation (sampled every 100 ps) ($n = 3$). (*C*) z-axis position of an A9C molecule. The simulations were run in presence of Ca^{2+} in the open-state model (red), 5OYB structure (yellow), and 5OYG (blue). (*D*) Contact probability across three repeats in the last 100 ns of the 200-ns simulation trajectory of residues shown in *A*. Individual repeats are shown as individual data points; horizontal lines denote mean values. (*E*) (*i*) Whole-cell currents recorded from HEK-293T cells expressing TMEM16A, TMEM16A-S513A, -V539A, -I636A, -K641A, or -Q645A channels, as indicated. Extracellular A9C (300 μM) was applied as indicated by the horizontal bar ("concentration jump"). Dashed horizontal lines indicate the zero-current level. (*ii*) Mean current inhibition (I_b/I_0) or (*iii*) current activation (I_a/I_0) plotted as box plot for each channel type, as indicated. The number of experiments was 5 to 9 in each case. *$P < 0.05$, compared to TMEM16A.

overexpressed in pulmonary arteries during pulmonary hypertension (45), and up-regulation of Cl^- currents has been implicated in the proliferation of pulmonary artery smooth-muscle cells (46). TMEM16A blockers could provide a therapeutic benefit in pulmonary hypertension by both inducing smooth-muscle relaxation and possibly by reducing cell proliferation. TMEM16A blockers might also be employed in the treatment of diseases of altered tone of the cerebral microcirculation such as ischemic stroke and Alzheimer's disease (47). Small molecules that activate the TMEM16A channel could be used in cystic fibrosis (48, 49), where TMEM16A activators may promote Cl^- fluxes in epithelial cells in which CFTR channels are defective. In general, modulators that, like A9C, act at depolarized V_m by entering into the channel pore may be especially effective for the control of TMEM16A in excitable cells, including nociceptive neurons, where TMEM16A is a proposed target for pain (50). Another target for voltage-dependent modulators of

TMEM16A may be the detrusor smooth muscle (51), in which the V_m may go above 0 mV during micturition, and TMEM16A inhibition may be beneficial in overactive bladder treatment. Our determination of a putative binding site for A9C may offer avenues for rational drug design targeted to this region of the channel and the development of therapeutic drugs.

Methods

Detailed descriptions of cell culturing, single-point mutagenesis, electrophysiology, generation of molecular models of TMEM16A, and MD simulations are included in *SI Appendix*.

Electrophysiology. Wild-type and mutant mouse TMEM16A (isoform *a*) subcloned into the pcDNA3.1 vector were transiently transfected into Human embryonic kidney 293T (HEK-293T) cells. TMEM16A currents were recorded with wholecell or inside-out configuration of the patch-clamp technique (17, 18). The exchange of solutions was achieved by using a local perfusion system consisting of

eight tubes of 1.2-mm diameter, into which the tip of the patch pipette was inserted or using an ultra-rapid (<50 ms) computer-controlled perfusion system (Warner Instruments, Hamden, CT). Composition of solutions and stimulation protocols are detailed in *SI Appendix*.

Molecular Modeling. Molecular models of TMEM16A were generated using Modeler, and MD simulations were carried out with GROMACS version 2020.1. Analysis was performed using GROMACS version 2020.1, MDAnalysis, Visual Molecular Dynamics (VMD) version 1.9.3 and PyMOL version 2.0.

Statistical Analysis. Data are given as mean $\pm$ SEM, unless stated otherwise. Statistical significance was determined with two-tailed paired or unpaired *t* tests or one-way ANOVA with Bonferroni's post-test, as appropriate. For all statistical tests, *P* values <0.05 were considered significant.

Data Availability. The open-state molecular model of TMEM16A developed and used in this study can be accessed at https://zenodo.org/record/4655940. All other study data are included in the article and/or supporting information.

1. N. Pedemonte, L. J. Galietta, Structure and function of TMEM16 proteins (anoctamins). *Physiol. Rev.* **94**, 419–459 (2014).
2. A. Adomaviciene, K. J. Smith, H. Garnett, P. Tammaro, Putative pore-loops of TMEM16/anoctamin channels affect channel density in cell membranes. *J. Physiol.* **591**, 3487–3505 (2013).
3. S. R. Bushell *et al.*, The structural basis of lipid scrambling and inactivation in the endoplasmic reticulum scramblase TMEM16K. *Nat. Commun.* **10**, 3956 (2019).
4. E. Di Zanni, A. Gradogna, C. Picco, J. Scholz-Starke, A. Boccaccio, TMEM16E/ANO5 mutations related to bone dysplasia or muscular dystrophy cause opposite effects on lipid scrambling. *Hum. Mutat.* **41**, 1157–1170 (2020).
5. K. Yu *et al.*, Identification of a lipid scrambling domain in ANO6/TMEM16F. *eLife* **4**, e06901 (2015).
6. M. A. Kamaleddin, Molecular, biophysical, and pharmacological properties of calcium-activated chloride channels. *J. Cell. Physiol.* **233**, 787–798 (2018).
7. K. Kunzelmann *et al.*, TMEM16A in cystic fibrosis: Activating or inhibiting? *Front. Pharmacol.* **10**, 3 (2019).
8. U. Duvvuri *et al.*, TMEM16A induces MAPK and contributes directly to tumorigenesis and cancer progression. *Cancer Res.* **72**, 3270–3281 (2012).
9. D. Crottès, L. Y. Jan, The multifaceted role of TMEM16A in cancer. *Cell Calcium* **82**, 102050 (2019).
10. Y. Seo *et al.*, Ani9, a novel potent small-molecule ANO1 inhibitor with negligible effect on ANO2. *PLoS One* **11**, e0155771 (2016).
11. S. J. Oh *et al.*, MONNA, a potent and selective blocker for transmembrane protein with unknown function 16/anoctamin-1. *Mol. Pharmacol.* **84**, 726–735 (2013).
12. W. Namkung, Z. Yao, W. E. Finkbeiner, A. S. Verkman, Small-molecule activators of TMEM16A, a calcium-activated chloride channel, stimulate epithelial chloride secretion and intestinal contraction. *FASEB J.* **25**, 4048–4062 (2011).
13. M. Genovese *et al.*, TRPV4 and purinergic receptor signalling pathways are separately linked in airway epithelia to CFTR and TMEM16A chloride channels. *J. Physiol.* **597**, 5859–5878 (2019).
14. T. Kim *et al.*, Design of anticancer 2,4-diaminopyrimidines as novel anoctamin 1 (ANO1) ion channel blockers. *Molecules* **25**, 5180 (2020).
15. Y. Huang *et al.*, The natural compound cinnamaldehyde is a novel activator of calcium-activated chloride channel. *J. Membr. Biol.* **251**, 747–756 (2018).
16. H. L. Danahay *et al.*, TMEM16A potentiation: A novel therapeutic approach for the treatment of cystic fibrosis. *Am. J. Respir. Crit. Care Med.* **201**, 946–954 (2020).
17. C. M. Ta, A. Adomaviciene, N. J. Rorsman, H. Garnett, P. Tammaro, Mechanism of allosteric activation of TMEM16A/ANO1 channels by a commonly used chloride channel blocker. *Br. J. Pharmacol.* **173**, 511–528 (2016).
18. C. M. Ta, K. E. Acheson, N. J. G. Rorsman, R. C. Jongkind, P. Tammaro, Contrasting effects of phosphatidylinositol 4,5-bisphosphate on cloned TMEM16A and TMEM16B channels. *Br. J. Pharmacol.* **174**, 2984–2999 (2017).
19. S. C. Le, Z. Jia, J. Chen, H. Yang, Molecular basis of PIP$_2$-dependent regulation of the Ca^{2+}-activated chloride channel TMEM16A. *Nat. Commun.* **10**, 3769 (2019).
20. N. K. Lim, A. K. M. Lam, R. Dutzler, Independent activation of ion conduction pores in the double-barreled calcium-activated chloride channel TMEM16A. *J. Gen. Physiol.* **148**, 375–392 (2016).
21. G. Jeng, M. Aggarwal, W.-P. Yu, T.-Y. Chen, Independent activation of distinct pores in dimeric TMEM16A channels. *J. Gen. Physiol.* **148**, 393–404 (2016).
22. C. Paulino, V. Kalienkova, A. K. M. Lam, Y. Neldner, R. Dutzler, Activation mechanism of the calcium-activated chloride channel TMEM16A revealed by cryo-EM. *Nature* **552**, 421–425 (2017).
23. S. Dang *et al.*, Cryo-EM structures of the TMEM16A calcium-activated chloride channel. *Nature* **552**, 426–429 (2017).
24. C. J. Peters *et al.*, The sixth transmembrane segment is a major gating component of the TMEM16A calcium-activated chloride channel. *Neuron* **97**, 1063–1077.e4 (2018).
25. A. K. Lam, R. Dutzler, Calcium-dependent electrostatic control of anion access to the pore of the calcium-activated chloride channel TMEM16A. *eLife* **7**, e39122 (2018).
26. B.-C. Lee *et al.*, Gating mechanism of the extracellular entry to the lipid pathway in a TMEM16 scramblase. *Nat. Commun.* **9**, 3251 (2018).
27. J. Tien *et al.*, A comprehensive search for calcium binding sites critical for TMEM16A calcium-activated chloride channel activity. *eLife* **3**, e02772 (2014).
28. Z. Jia, J. Chen, Specific PIP$_2$ binding promotes calcium activation of TMEM16A chloride channels. *Commun. Biol.* **4**, 259 (2021).
29. C. J. Peters *et al.*, Four basic residues critical for the ion selectivity and pore blocker sensitivity of TMEM16A calcium-activated chloride channels. *Proc. Natl. Acad. Sci. U.S.A.* **112**, 3547–3552 (2015).
30. C. Paulino *et al.*, Structural basis for anion conduction in the calcium-activated chloride channel TMEM16A. *eLife* **6**, e26232 (2017).
31. A. K. M. Lam, R. Dutzler, Mechanism of pore opening in the calcium-activated chloride channel TMEM16A. *Nat. Commun.* **12**, 786 (2021).
32. A. K. M. Lam, J. Rheinberger, C. Paulino, R. Dutzler, Gating the pore of the calcium-activated chloride channel TMEM16A. *Nat. Commun.* **12**, 785 (2021).
33. N. B. Last, T. Kolmakova-Partensky, T. Shane, C. Miller, Mechanistic signs of double-barreled structure in a fluoride ion channel. *eLife* **5**, e18767 (2016).
34. C. Miller, Open-state substructure of single chloride channels from Torpedo electroplax. *Philos. Trans. R. Soc. Lond. B Biol. Sci.* **299**, 401–411 (1982).
35. V. Kalienkova *et al.*, Stepwise activation mechanism of the scramblase nhTMEM16 revealed by cryo-EM. *eLife* **8**, e44364 (2019).
36. G. Khelashvili *et al.*, Dynamic modulation of the lipid translocation groove generates a conductive ion channel in Ca^{2+}-bound nhTMEM16. *Nat. Commun.* **10**, 4972 (2019).
37. T. Jiang, K. Yu, H. C. Hartzell, E. Tajkhorshid, Lipids and ions traverse the membrane by the same physical pathway in the nhTMEM16 scramblase. *eLife* **6**, e28671 (2017).
38. D. Colquhoun, Binding, gating, affinity and efficacy: The interpretation of structure-activity relationships for agonists and of the effects of mutating receptors. *Br. J. Pharmacol.* **125**, 924–947 (1998).
39. R. Estévez, B. C. Schroeder, A. Accardi, T. J. Jentsch, M. Pusch, Conservation of chloride channel structure revealed by an inhibitor binding site in ClC-1. *Neuron* **38**, 47–59 (2003).
40. A. J. Davis *et al.*, Expression profile and protein translation of TMEM16A in murine smooth muscle. *Am. J. Physiol. Cell Physiol.* **299**, C948–C959 (2010).
41. B. Manoury, A. Tamuleviciute, P. Tammaro, TMEM16A/anoctamin 1 protein mediates calcium-activated chloride currents in pulmonary arterial smooth muscle cells. *J. Physiol.* **588**, 2305–2314 (2010).
42. C. Heinze *et al.*, Disruption of vascular Ca^{2+}-activated chloride currents lowers blood pressure. *J. Clin. Invest.* **124**, 675–686 (2014).
43. C. Thomas-Gatewood *et al.*, TMEM16A channels generate Ca^{2+}-activated Cl$^−$ currents in cerebral artery smooth muscle cells. *Am. J. Physiol. Heart Circ. Physiol.* **301**, H1819–H1827 (2011).
44. B. Wang, C. Li, R. Huai, Z. Qu, Overexpression of ANO1/TMEM16A, an arterial Ca^{2+}-activated Cl$^−$ channel, contributes to spontaneous hypertension. *J. Mol. Cell. Cardiol.* **82**, 22–32 (2015).
45. H. Sun, Y. Xia, O. Paudel, X. R. Yang, J. S. Sham, Chronic hypoxia-induced upregulation of Ca^{2+}-activated Cl$^−$ channel in pulmonary arterial myocytes: A mechanism contributing to enhanced vasoreactivity. *J. Physiol.* **590**, 3507–3521 (2012).
46. W. Liang, J. B. Ray, J. Z. He, P. H. Backx, M. E. Ward, Regulation of proliferation and membrane potential by chloride currents in rat pulmonary artery smooth muscle cells. *Hypertension* **54**, 286–293 (2009).
47. J. Cheng *et al.*, Targeting pericytes for therapeutic approaches to neurological disorders. *Acta Neuropathol.* **136**, 507–523 (2018).
48. J. Ousingsawat *et al.*, Loss of TMEM16A causes a defect in epithelial Ca2+-dependent chloride transport. *J. Biol. Chem.* **284**, 28698–28703 (2009).
49. J. R. Rock *et al.*, Transmembrane protein 16A (TMEM16A) is a Ca^{2+}-regulated Cl$^−$ secretory channel in mouse airways. *J. Biol. Chem.* **284**, 14875–14880 (2009).
50. X. Jin *et al.*, Activation of the Cl$^−$ channel ANO1 by localized calcium signals in nociceptive sensory neurons requires coupling to the IP$_3$ receptor. *Sci. Signal.* **6**, ra73 (2013).
51. D. A. Bijos, M. J. Drake, B. Vahabi, Anoctamin-1 in the juvenile rat urinary bladder. *PLoS One* **9**, e106190 (2014).

www.manaraa.com